

Crustal magnetic fields do not lead to large magnetic-field amplifications in binary neutron-star mergers

MICHAEL CHABANOV,¹ SAMUEL D. TOOTLE,¹ ELIAS R. MOST,^{2,3,4} AND LUCIANO REZZOLLA^{1,5,6}

¹*Institut für Theoretische Physik, Goethe Universität, Max-von-Laue-Str. 1, 60438 Frankfurt am Main, Germany*

²*Princeton Center for Theoretical Science, Princeton University, Princeton, NJ 08544, USA*

³*Princeton Gravity Initiative, Princeton University, Princeton, NJ 08544, USA*

⁴*School of Natural Sciences, Institute for Advanced Study, Princeton, NJ 08540, USA*

⁵*Frankfurt Institute for Advanced Studies, Ruth-Moufang-Str. 1, 60438 Frankfurt am Main, Germany*

⁶*School of Mathematics, Trinity College, Dublin 2, Ireland*

ABSTRACT

The amplification of magnetic fields plays an important role in explaining numerous astrophysical phenomena associated with binary neutron-star mergers, such as mass ejection and the powering of short gamma-ray bursts. Magnetic fields in isolated neutron stars are often assumed to be confined to a small region near the stellar surface, while they are normally taken to fill the whole stars in the numerical modelling. By performing high-resolution, global, and high-order general-relativistic magnetohydrodynamic simulations we investigate the impact of a purely crustal magnetic field and contrast it with the standard configuration consisting of a dipolar magnetic field with the same magnetic energy but filling the whole star. While the crust-configurations are very effective in generating strong magnetic fields during the Kelvin-Helmholtz-instability stage, they fail to achieve the same level of magnetic-field amplification of the full-star configurations. This is due to the lack of magnetized material in the neutron-star interiors to be used for further turbulent amplification and to the surface losses of highly magnetized matter in the crust-configurations. Hence, the final magnetic energies in the two configurations differ by more than one order of magnitude. We briefly discuss the impact of these results on astrophysical observables and how they can be employed to deduce the magnetic topology in merging binaries.

Keywords: stars: neutron — stars: magnetic field — magnetohydrodynamics (MHD) — methods: numerical

1. INTRODUCTION

The coincident detection of the gravitational-wave signal GW170817, of the short gamma-ray burst GRB 170817A and of the kilonova AT2017gfo (Abbott et al. 2017; Drout et al. 2017; Cowperthwaite et al. 2017) has provided strong evidence that short gamma-ray bursts are related to binary neutron-star (BNS) mergers and that magnetic fields play an important role in the post-merger evolution. This conclusion stems from a series of studies identifying magnetic fields as crucial to generate magnetically driven outflows (Kiuchi et al. 2012; Siegel et al. 2013; Kiuchi et al. 2018; Fernández et al. 2019; Ciolfi 2020a; Fujibayashi et al. 2023), but also to produce the conditions necessary for jet formation and launching (Liu et al. 2008; Anderson et al. 2008; Rezzolla et al. 2011; Palenzuela et al. 2013; Kiuchi et al. 2015b; Murguía-Berthier et al. 2016; Ciolfi 2020b; Nathanail et al. 2020, 2021; Gottlieb et al. 2022).

Early studies identified that turbulence, starting from the Kelvin-Helmholtz instability (KHI) triggered in the first few milliseconds after merger by the shearing of the stellar surfaces, is essential in the amplification of the magnetic field (Price & Rosswog 2006; Giacomazzo et al. 2011; Kiuchi

et al. 2015a; Aguilera-Miret et al. 2020). However, because the accurate description of the turbulent motions can only be achieved at enormous computational cost, a number of suggestions have been made over the years to obtain a subgrid-scale modeling of the magnetic-field evolution. These so-called “large-eddy simulations” (LESs) have attempted to incorporate the small-scale, dynamo-driven, magnetic-field amplification into *global* high-resolution general-relativistic magnetohydrodynamics (GRMHD) simulations employing computationally affordable resolutions (Giacomazzo et al. 2015; Palenzuela et al. 2015; Radice 2017; Aguilera-Miret et al. 2020). At the same time, *local* and high-resolution simulations of KHI-driven turbulence have shown evidence of possible converged and saturated magnetic-field amplification (see, e.g., Zrake & MacFadyen 2013; Obergaulinger et al. 2010).

While a generally accepted view of the process of magnetic-field amplification is still missing, broad consensus is present that the maximum achievable magnetic-field strength is reached by an equipartition between the magnetic energy and the kinetic energy on the smallest scales, thus yielding “magnetar-strength” fields of the order \gtrsim

10^{16} G (see, e.g., Price & Rosswog 2006; Liu et al. 2008; Giacomazzo et al. 2009, for some initial estimates). This expectation, which has so far been difficult to demonstrate via direct global simulations, has recently been shown to hold at least with high-resolution LES simulations by Palenzuela et al. (2022), where the amplification of the averaged magnetic field saturated to approximately 10^{16} G.

A distinct but equally interesting question is that regarding the role played by the initial magnetic-field strength and topology (see Giacomazzo et al. 2009; Kawamura et al. 2016; Ruiz et al. 2020, for some initial investigations). Following a long list of works in this area, Aguilera-Miret et al. (2022) have recently found that the initial magnetic-field topology is quickly destroyed and that the final turbulent state depends only weakly on the configuration considered, e.g., dipoles with different strengths, misaligned dipoles, and even a multipolar structure. A common thread in all of these studies is the assumption that the magnetic fields are confined to the neutron stars and permeating the whole stellar structure. Yet, a number of works exploring the rotational, thermal, and magnetic evolution of neutron stars have considered as most natural those configurations in which the magnetic field is concentrated only in the crust (see, e.g., Pons & Geppert 2007; Pons et al. 2009). This configuration follows from assuming the stellar core as a type-I superconductor that expels most of its magnetic flux on a very short timescale (see also Viganò et al. 2021). Here, we explore a BNS scenario in which, by the time of the merger, the magnetic fields in the stellar cores have been expelled or have decayed, so that only crustal fields are present. If such configurations are indeed common in neutron stars, and since the stellar crusts play a fundamental role in the development of the KHI, it is interesting to assess whether strong crustal magnetic fields lead to a distinct amplification process and to a different gravitational-wave signal.

To address this question, we report the results of high-resolution, global, and high-order GRMHD simulations of merging BNSs with two different initial magnetic-fields topologies. More specifically, in addition to the standard configuration with a dipolar magnetic field filling the whole star, we consider a configuration where the magnetic field is still dipolar and has the *same* total magnetic energy, but is confined to the crust only. Overall, our simulations indicate that such “crust-configurations” fail to produce a sufficiently large turbulent amplification of the magnetic field and lead to a post-merger hypermassive neutron star (HMNS) with an amplified electromagnetic energy that is $\lesssim 5\%$ of the corresponding “full-configurations”.

2. MATHEMATICAL AND NUMERICAL METHODS

The simulations reported below are obtained after solving the Einstein equations together with those of ideal

GRMHD via the high-order high-resolution shock-capturing code FIL (Most et al. 2019, 2020) and the temperature-dependent equation of state TNTYST, which has a maximum mass of $M_{\text{TOV}} = 2.21 M_{\odot}$ (Togashi et al. 2017). To assess whether the resolution employed is sufficient to capture the relevant physical behaviour, we employ two different resolutions on the highest (7th) refinement level with $\Delta x \sim 0.047 M_{\odot} \approx 70$ m, or of $\Delta x \sim 0.071 M_{\odot} \approx 105$ m; we note that although these are not the highest resolutions employed so far in the literature (see, e.g., Siegel et al. 2013; Kiuchi et al. 2018), they benefit from the use of a high-order code (Most et al. 2019). Hereafter, we will refer to these two setups respectively as high (HR) and low (LR) resolutions, but discuss the results of the former only; details on the LR results and their differences with the HR ones are presented in the Appendix. We note that although the resolutions employed here are very high, the magnetorotational instability (MRI) is normally under-resolved for most of the matter in our simulations as estimated via different MRI quality factors (Siegel et al. 2013; Kiuchi et al. 2018). However, we expect the MRI to have a little impact on the results obtained here and for two different reasons. First, the MRI would develop only in a region where $\partial_{\varpi}\Omega < 0$, where Ω and ϖ are respectively the angular velocity and the distance from the rotation axis; however the large shear produced at the merger and the subsequent turbulence that follows prevent the development of a coherent angular velocity profile in the merged object at least initially. Second, because even when a coherent angular velocity profile is developed, the MRI would have the same impact on both configurations since the region where $\partial_{\varpi}\Omega < 0$ is very similar and with comparable magnetic-field strengths in the two cases.

In both the “full-” and “crust-configurations”, the magnetic-field is initialized via the vector potential as $A_i = A_b [- (x^j - x_{\text{NS}}^j) \epsilon_{ij}] \exp[-g_w(r - g_r)^2] \max(p - p_{\text{co}}, 0)^n$ for $i = x, y$ and $A_z = 0$, where x_{NS}^j denote the coordinate centers of the two stars ($x_{\text{NS}}^3 = z_{\text{NS}} = 0$), $r := \sqrt{\delta_{ij}(x^i - x_{\text{NS}}^i)(x^j - x_{\text{NS}}^j)}$, and ϵ_{ij} is the Levi-Civita symbol. The magnetized region extends outwards to the radius where the pressure reaches the cut-off pressure $p_{\text{co}} \approx 6 \times 10^{-5} \times p_c$, where p_c is the central pressure, and inwards to the radius R_{in} , such that $A_i = 0$ if $r < R_{\text{in}}$ (see Table 1 in the Appendix for additional details on the seeding parameters).

With such a prescription, the initial magnetic field has closed loops around a neutral line that is at $\simeq 0.52 R_{\text{NS}}$ for the full-configurations, while it is at $\simeq 0.87 R_{\text{NS}}$ for the crust-configurations (a view of the magnetic-field topology soon before merger is shown in Fig. 5 in the Appendix). For the high (low) resolutions, the magnetized crust is resolved with $\gtrsim 17$ ($\gtrsim 11$) gridpoints and does not suffer from significant numerical dissipation in the remainder of the inspi-

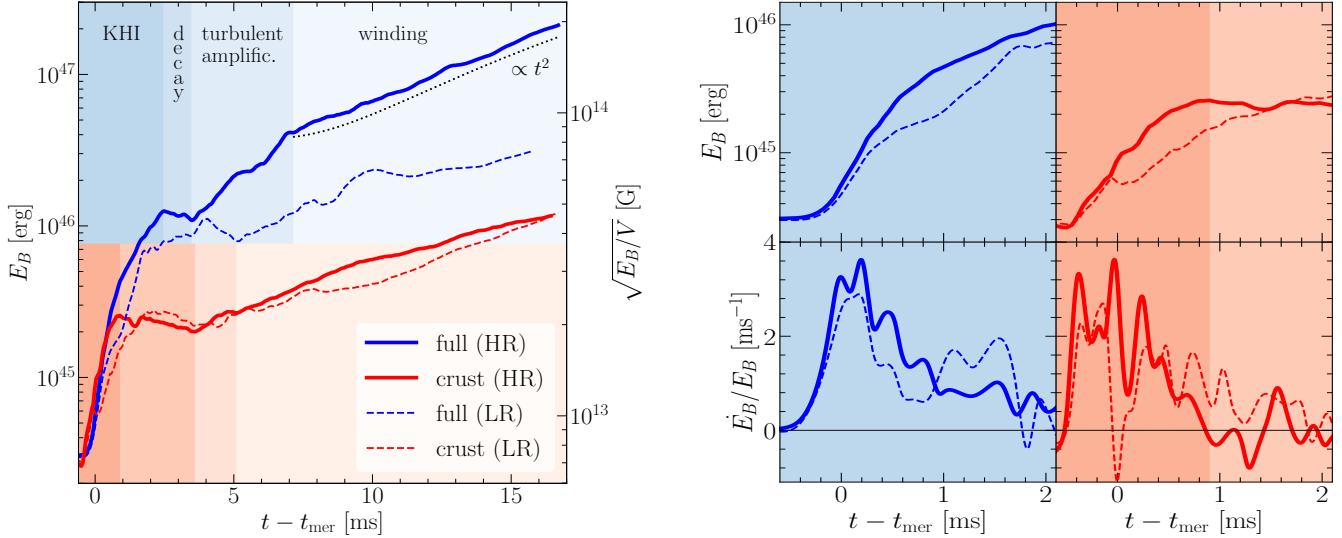


Figure 1. *Left:* Evolution of the total magnetic energy E_B for the high-resolution (HR) full- (blue solid line) and crust-configuration (red solid line); dashed blue (red) lines refer to the low-resolution (LR) full- and crust-configuration, respectively. Different shadings highlight the four stages of the evolution. The black dotted line shows a quadratic fit to full (HR) in the winding stage and is shifted downwards for better visualization. The quantity V denotes the reference volume of a sphere with a radius of 11 km. *Right top:* The same as in the left but for $t - t_{\text{mer}} \lesssim 2$ ms. *Right bottom:* the same as the top but for the growth-rate \dot{E}_B/E_B .

ral. Finally, we note that to reduce diffusion during the inspiral, the magnetic fields are seeded when the separation between the stars decreases below $8.9 M_{\odot}$, which corresponds to $t - t_{\text{mer}} \lesssim -1$ ms.

3. RESULTS

We start by describing the overall dynamics with particular focus on the difference between the full and crust-configurations relative to the magnetic-field amplification. In the left panel of Fig. 1 we report the evolution of the total electromagnetic energy in the whole computational domain \mathcal{V} , $E_B := \int_{\mathcal{V}} d^3x \sqrt{\gamma} (E^2 + B^2) / 8\pi$, where γ is the determinant of the three-metric, and $B^2 := B_i B^i$ ($E^2 := E_i E^i$) is the square modulus of the magnetic (electric) field in the Eulerian frame. The different lines refer to the crust- (red) and full-configurations (blue), with dashed and solid lines reporting the behaviour of the low- (LR) and high-resolution (HR) simulations, respectively. Note that all configurations start with the *same* electromagnetic energy of $\sim 3 \times 10^{44}$ erg, corresponding to a maximum initial magnetic-field strength of $\sim 10^{14}$ G ($\sim 2.4 \times 10^{14}$ G) for the full-configuration (crust-configuration; see also Table 1).

To describe such a complex dynamics, it is convenient to classify the evolution of E_B in four distinct stages that are highlighted by different shadings in Fig. 1. The first stage of the evolution, or “KHI-driven stage”, begins when tidal forces start significantly deforming both stars, at $t - t_{\text{mer}} \approx -0.6$ ms (-0.6), and ends when the KHI-driven turbulence ceases to increase E_B at $t - t_{\text{mer}} \approx 2.46$ ms (0.9) for the full-

(crust-) configuration¹. The KHI-unstable shear layer can be seen in the first column of Fig. 2, which presents cross-sections of the norm of the magnetic field $|B| := \sqrt{B^i B_i}$ in the (x, y) -plane at time $t - t_{\text{mer}} = -0.12$ ms and at an elevation² of $z \simeq 1$ km $\lesssim 0.115 R_{\text{NS}}$ for the full- (top row) and crust-configuration (bottom row). The second column of Fig. 2, at $t - t_{\text{mer}} = 0.52$ ms, highlights how the KHI-driven turbulent motion at the interface between the stars extends to other regions and involves also the stellar interiors. At this point, the amplification of the magnetic field has almost ended for the crust-configuration, as can be appreciated from the left panel of Fig. 1.

The second stage of the evolution, or “decay stage”, is instead characterized by a lack of amplification and the evolution of E_B is constant in time or exhibits a weak decay. This is the result of a combination of factors: the expansion of the dense HMNS core ($\rho \gtrsim 10^{13}$ gm/cm³), the ejection of matter at the HMNS surface, and an insufficient magnetic-field amplification. During this stage, magnetic pressure gradients accelerate the expansion of matter in the remnant and hence are doing work on the fluid. At the same time, the KHI-driven turbulent motion ceases to be produced efficiently as the kinetic energy in the remnant is reduced through the emission of gravitational waves, shock-heating and matter ejec-

¹ A more careful examination of Fig. 1 and 2 reveals that there are two different phases in the KHI-driven stage with slightly different growth-rates; for simplicity, we will ignore these small differences.

² We use this elevation to minimise the influence of the boundary conditions across the equatorial plane; smaller elevations yield very similar views.

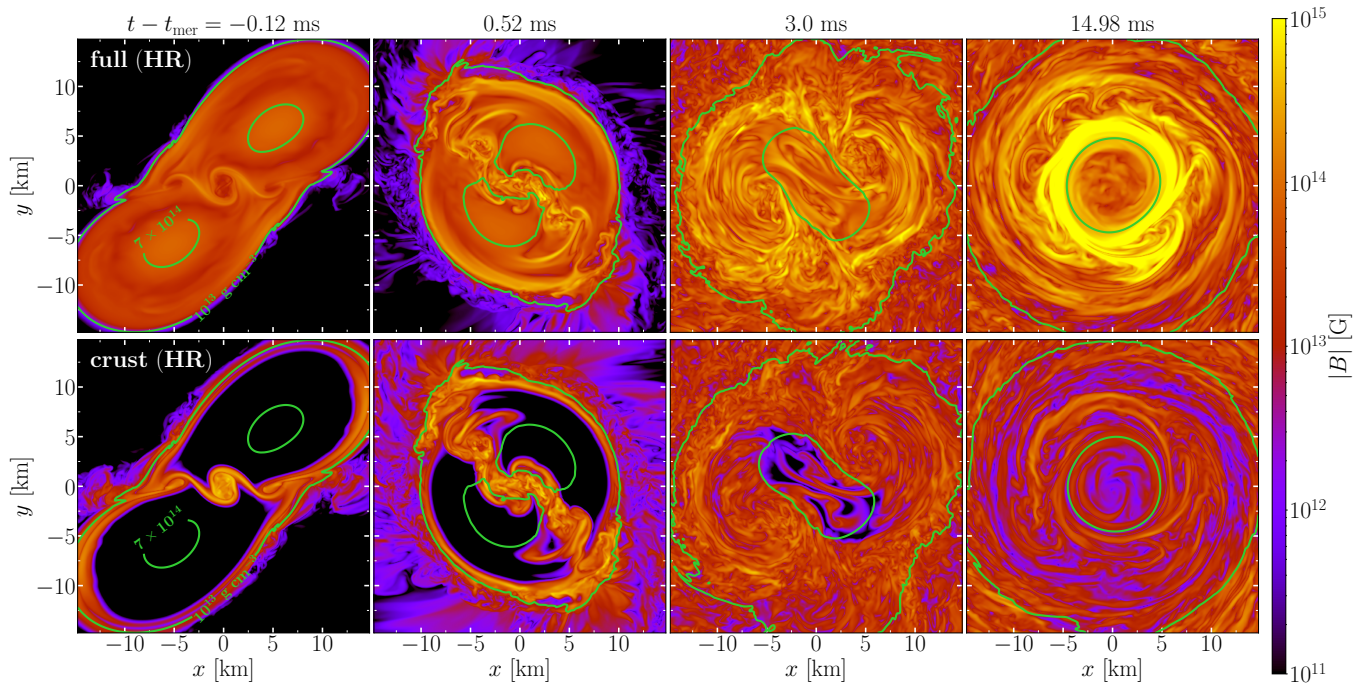


Figure 2. Distributions on the (x, y) plane of the magnetic-field strength $|B|$ from the HR simulations at four representative times. The top and bottom rows refer to the full- and crust-configurations, respectively.

tion. This leads to an overall decrease in the electromagnetic energy. It is interesting to note that during this stage, the lack of turbulence in the HMNS core results in the magnetic fields of the crust-configurations to remain very weak and the full-configuration to preserve its initial large-scale coherence; this can be seen in the third column of Fig. 2 at $t - t_{\text{mer}} = 3$ ms. The decay stage ends for the full- (crust-) configuration at $t - t_{\text{mer}} = 3.48$ ms (3.59).

The third stage, or “turbulent-amplification stage”, is characterized by a new process of magnetic-field amplification that becomes strong enough to counteract the decay of the previous stage and leads to a net amplification (see also the high-resolution calculations of Siegel et al. 2013). At this point in the evolution, the HMNS has emerged from the highly nonlinear early post-merger phase in which the two stellar cores collide and bounce (see Takami et al. 2015, for a toy model). Subsequent turbulent motions can develop and lead to a nonlinear amplification of the magnetic field – with a smaller growth-rate than in the KHI stage and not related to the development of the MRI – that result into a substantial growth of the poloidal field up to $t - t_{\text{mer}} = 7.13$ ms (5.09).

The fourth and final stage, or “winding stage”, starts when the turbulence is fully developed and more regular, large-scale shearing motions can be produced in the HMNS. Under the infinite-conductivity conditions of ideal-MHD, these motions lead to the well-known linear-in-time growth of the magnetic field that represents the quasi-stationary state reached in our simulations (see the final part of the Fig. 1 and the fourth column of Fig. 2). Obviously, the winding

stage cannot continue indefinitely, but will terminate when the magnetic-field energy is in equipartition with the kinetic energy stored in the differential rotation, so that further amplification is energetically disfavoured. We should note that the classification discussed here describes well the dynamics in our simulations, which have moderate initial magnetic fields. However, if the initial exponential amplification is much larger – as a result of additional driving terms in the MHD equations (Giacomazzo et al. 2015; Palenzuela et al. 2022) or of very large initial magnetic fields (Kiuchi et al. 2018) – equipartition may be reached much earlier and the subsequent stages may be absent (see Kiuchi et al. 2018; Giacomazzo et al. 2015; Palenzuela et al. 2022, where these stages are not found).

While the dynamics and stage classification presented so far applies to both crust- and full-configurations, important differences are present that ultimately determine the final magnetic-field amplification. In particular, the KHI-driven evolution is very efficient in the crust-configuration but also ends earlier than for the full-configuration, thus achieving a smaller magnetic-field amplification. In addition, the KHI is followed by a longer decay stage and a shorter turbulent amplification (see red solid line in the left panel of Fig. 1). As a result, when the winding stage starts for the crust-configuration, the magnetic energy is about one order of magnitude smaller than in the full-configuration; since the growth-rates are comparable in the two topologies, this difference remains unchanged till the end of the simulations. Also worth noting is that the turbulent amplifi-

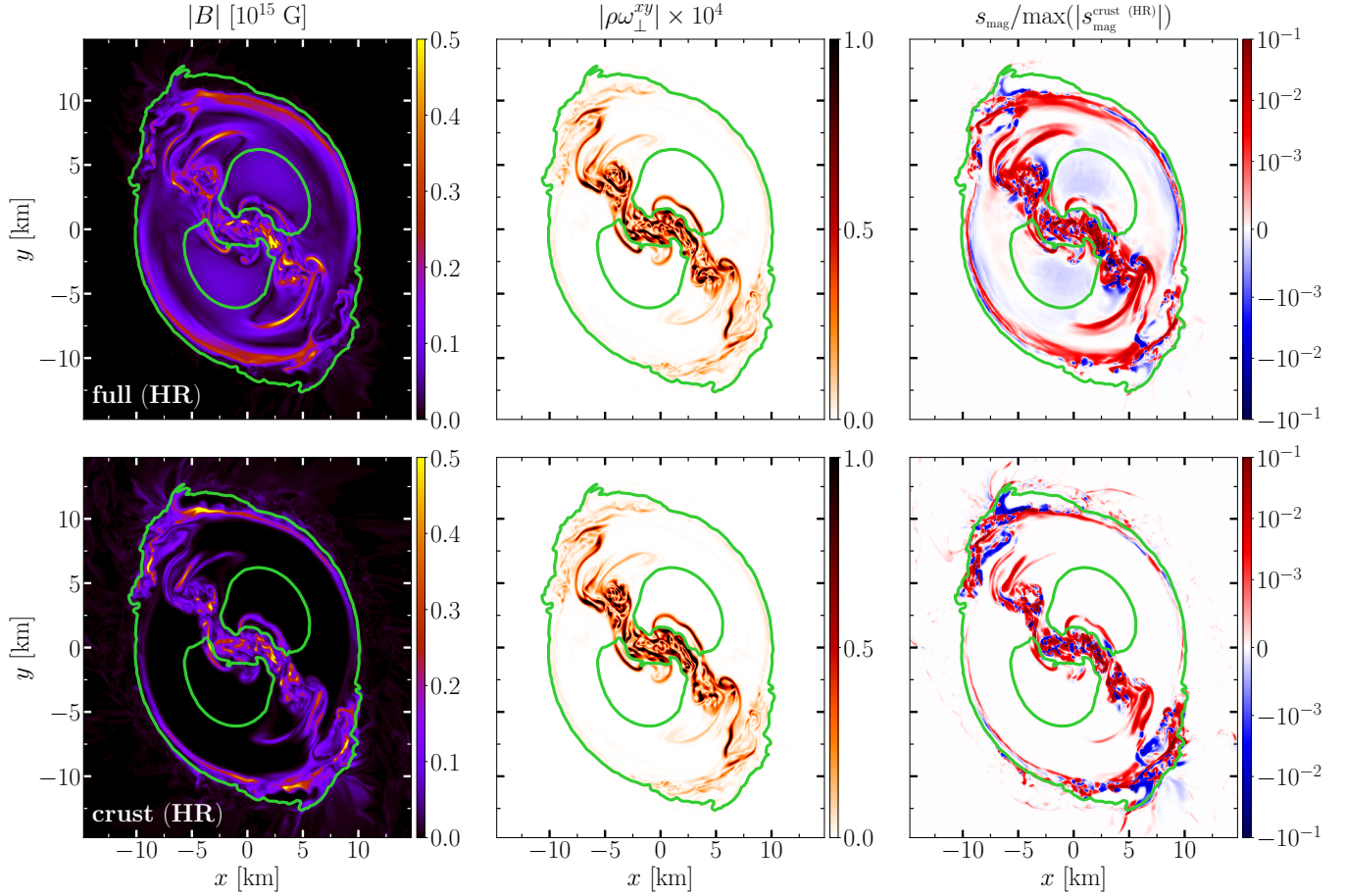


Figure 3. Distributions on the (x, y) plane of the magnetic-field strength $|B|$ (left column), of the density-weighted xy -component of the kinematic vorticity $|\rho\omega_{\perp}^{xy}|$ (middle column), and of the amplification source term s_{mag} (right column) at $t - t_{\text{mer}} = 0.52$ ms. The top and bottom rows refer to the full- and crust-configurations, respectively.

ation is smaller in the crust-configuration as the result of two combined effects. First, a smaller amount of magnetised matter is subject to turbulent motions. Second, because the magnetised matter is only at lower densities (i.e., $\rho \lesssim 10^{13} \text{ gm/cm}^3$) and near the stellar surface, a good portion of it is shed in the external medium before it can be amplified further. These “winds”, that are in good part (but not exclusively) magnetically driven, are the result of large deviations from a magnetohydrostatic equilibrium at the remnant surface and are made more violent by the presence of comparatively stronger magnetic fields in the crust configuration. By contrast, the amplification in the full-configuration can benefit from larger volumes of magnetised matter and smaller losses of magnetized matter at the surface, where the pressure gradients are comparatively smaller.

The right panel of Fig. 1 gives us the opportunity to discuss in more detail the turbulent magnetic-field amplification during the first two stages of the evolution and thus for $t - t_{\text{mer}} \lesssim 2$ ms. In particular, shown in the upper parts is the evolution of E_B for the same configurations in the left panel, while the lower parts report the corresponding nor-

malized growth-rate \dot{E}_B/E_B . First, an exponential growth is present at the onset of magnetic-field amplification, which then reaches its maximum value in $\lesssim 0.2$ ms (0.7) for the crust- (full-) configuration. While the maximum growth-rates of the two configurations are comparable for the same resolution, the changes in E_B are considerably more rapid in the crust-configuration, as it is natural to expect since the magnetic energy involved in the KHI amplification is confined to a smaller volume and nearly all of the initial electromagnetic energy participates in the amplification process as the KHI develops. After the maximum of \dot{E}_B/E_B has been reached, the subsequent evolution is qualitatively very similar in all configurations. In particular, the growth-rate decays until it reaches negative values and the KHI-driven stage ends. During this decay, very short variations of the growth-rate take place with a period of $\simeq 0.25 - 0.35$ ms; considering an eddy-rotation velocity of $\sim 0.15c$, this variation yields eddy lengthscales of $\sim 1.8 - 2.5$ km, which match well the size of the largest eddies produced across all simulations. This suggests that the decay in the growth-rate is related to the largest eddy turnovers in the KHI-driven stage and the

periodic increase/decrease of the growth-rate is the result of the amplification and subsequent dissipation of large-scale flux tubes that are dragged into rotation by the largest eddies. Furthermore, due to periodic bounces of the two cores with a period of ~ 0.77 ms, the shear layer between the stars is turned over at half of this period and drives the production of the largest eddies. This dynamics highlights that a persistent amplification requires the development of a fully turbulent stellar interior. While this is almost inevitable in the case of the full-configuration, where magnetized material is present across the HMNS, continued amplification is difficult for the crust-configuration, where turbulent amplification is still present but it is accompanied by the mixing of magnetized and unmagnetized material. Such mixing, in addition to magnetized-matter losses at the HMNS surface, reduces the growth-rate and favours dissipation.

Figure 3 offers an alternative means of comparing the full- (top row) and crust-configurations (bottom row) in the KHI-driven stage by examining representative quantities at $t - t_{\text{mer}} = 0.52$ ms. From left to right we report: $|B|/[10^{15} \text{ G}]$, the kinematic vorticity $|\rho\omega_{\perp}^{xy}| := \rho h^x_{\mu} h^y_{\nu} \omega^{\mu\nu}$, and the amplification source term, $s_{\text{mag}} := b^{\mu} b^{\nu} \sigma_{\mu\nu} - b^2 \Theta/6$. Here h^{μ}_{ν} denotes the projector tensor onto spatial hypersurfaces in the 3+1 formalism (Rezzolla & Zanotti 2013), $\omega^{\mu\nu}$ the kinematic vorticity, b^{μ} the magnetic field in the fluid-frame, $\sigma_{\mu\nu}$ the shear tensor, and Θ the expansion scalar (see Chabanov et al. 2021, for definitions). The quantity s_{mag} is the general-relativistic counterpart of the quantity employed by (Obergaullinger et al. 2010) to measure the strength of local sources ($s_{\text{mag}} > 0$) and sinks ($s_{\text{mag}} < 0$) of electromagnetic energy.

First, when comparing $|B|$ between the two configurations (left column), it is apparent that the largest values of the magnetic-field strength can be found in the crust-configuration and that these are reached very close to the putative surface of the HMNS (marked with a green contour line at 10^{13} gm/cm^3), while the inner parts are essentially devoid of magnetic field with the exception of those regions that belonged to the stellar surface. Second, when looking at the vorticity (middle column), it is also clear that the difference between the two configurations is very small and that in both cases the turbulent motion is concentrated in the low-density regions and falls-off rapidly when moving towards the stellar interior where, again, the turbulence is present only in the regions which were on the stellar surface. Finally, when comparing the sources and sinks of magnetic energy (right column), it is possible to realize that in both cases the sources are larger than the sinks (hence the amplification), but also that a large portion of the sources in the crust-configuration are just about to be lost at the HMNS surface. It is exactly the shedding of this precious, highly magnetized material that will quench the further amplification of the crust-configuration and ultimately lead to smaller

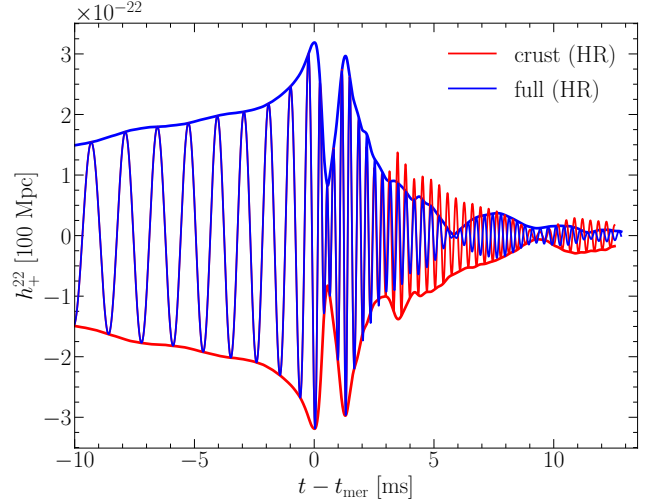


Figure 4. Gravitational-wave strain in the $\ell = 2, m = 2$ mode of the $+ -$ polarization extracted at ~ 740 km for a source at and normalized to a distance of 100 Mpc and for the two configurations. Thick solid lines report the corresponding amplitudes.

magnetic fields. The emission of neutrinos may further increase the strength of these winds, thus additionally reducing the potential of magnetic-field amplification in crust configurations.

We conclude our analysis by discussing the impact that the different magnetic-field topologies have on the emitted gravitational-wave signal, which we report in Fig 4. Note that the signals from the two configurations are indistinguishable during the inspiral and very similar over the first two milliseconds after the merger, when the KHI is most active. However, after $t - t_{\text{mer}} \gtrsim 2$ ms the waveforms differ considerably both in phase and amplitude, with the latter being smaller for the full-configuration. This is because the production of magnetic fields comes at the cost of the kinetic energy of the system in the full-configuration. In addition, the strong amplification of the magnetic field in the full-configuration reduces the $m = 2$ deformations leading to a more axisymmetric HMNS in the full-configuration and hence to a weaker gravitational-wave signal.

4. CONCLUSIONS

Motivated by a commonly assumed scenario in which magnetic fields in neutron stars are confined to a small region near the stellar surface, we have performed high-resolution, global, and high-order GRMHD simulations of merging BNSs with different initial magnetic-field topologies. In particular, while keeping the magnetic energy the same, we have investigated the impact of a purely *crustal* magnetic field and contrasted it with the standard configuration consisting of a dipolar magnetic field filling the whole star.

The use of high spatial resolution, high-order methods, and realistic initial magnetic fields has allowed us to highlight the presence of four distinct stages in the evolution of the magnetic field. While these stages are common to both configurations, and although the crust-configurations are more efficient in generating strong magnetic fields during the KHI-driven stage, we find that crust-configurations fail to achieve the same level of magnetic-field amplification as their full counterparts. We attribute this behaviour to the lack of magnetized material in the neutron-star interiors that can be used for further amplification and to the losses at the stellar surface of highly magnetized matter that afflicts the crust-configurations. As a result, by the end of our simulations the magnetic energies in the two configurations differ by a bit more than an order of magnitude and the gravitational-wave signal in the full-configuration is $\sim 50\%$ weaker than in the crustal counterpart as a result of a larger degree of axisymmetry.

Inevitably for global fully general-relativistic simulations of this type, ours also suffers from resolutions that, while very high and computationally expensive, are insufficient to capture a fully convergent behaviour during the KHI-driven exponential growth. However, by performing simulations with different resolutions we have verified that the behaviour presented here is only quantitatively modified by resolution and that the qualitative features remain unaltered. Hence, we expect our results to provide a reasonably accurate description of the magnetic-field amplification for stars with realistic initial magnetic fields.

Our findings have at least two important implications. First, future observations providing evidence for the presence of magnetar-strength magnetic fields in the merger remnant will represent a clear indication that the magnetic-field topology before merger could not have been a purely crustal one. Second, since the main difference between the two configurations considered here is represented by the volume fraction endowed with magnetic field, it is possible to correlate the post-merger dynamics – both in terms of gravitational-wave emission and in ejected matter – to the fraction of stellar vol-

ume that is magnetized. We leave these investigations to future work.

ACKNOWLEDGMENTS

We thank Vasilis Mpisketzis for useful discussions. Partial funding comes from the GSI Helmholtzzentrum für Schwerionenforschung, Darmstadt as part of the strategic R&D collaboration with Goethe University Frankfurt, from the State of Hesse within the Research Cluster ELEMENTS (Project ID 500/10.006), by the ERC Advanced Grant “JETSET: Launching, propagation and emission of relativistic jets from binary mergers and across mass scales” (Grant No. 884631) and the Deutsche Forschungsgemeinschaft (DFG, German Research Foundation) through the CRC-TR 211 “Strong-interaction matter under extreme conditions” – project number 315477589 – TRR 211. LR acknowledges the Walter Greiner Gesellschaft zur Förderung der physikalischen Grundlagenforschung e.V. through the Carl W. Fueck Laureatus Chair. The simulations were performed on HPE Apollo HAWK at the High Performance Computing Center Stuttgart (HLRS) under the grant BNSMIC. ERM gratefully acknowledges support as the John A. Wheeler Fellow at the Princeton Center for Theoretical Science, the Princeton Gravity Initiative and the Institute for Advanced Study. ERM acknowledges support through the Extreme Science and Engineering Discovery Environment (XSEDE) through Expanse at SDSC and Bridges-2 at PSC through allocations PHY210053 and PHY210074. ERM further acknowledge supported by Princeton Research Computing, a consortium of groups including the Princeton Institute for Computational Science and Engineering (PICSciE) and the Office of Information Technology’s High Performance Computing Center and Visualization Laboratory at Princeton University.

Software: Einstein Toolkit (Löffler et al. 2012), Carpet (Schnetter et al. 2004), FIL (Most et al. 2019), FUKA (Papenfort et al. 2021), Kadath (Grandclement 2010), ComPOSE (<https://compose.obspm.fr>)

APPENDIX

SIMULATIONS DETAILS AND IMPACT OF RESOLUTION

In what follows we provide additional details on the features of the simulations reported in the main text, as well as a discussion of how the amplification differs when considering lower resolutions. In particular, we recall that the simulations have been performed with the FIL code, which employs fourth-order accurate finite-difference stencils in Cartesian coordinates for the evolution of the constraint damping formulation of the Z4 formulation of the Einstein equations (Bernuzzi & Hilditch 2010; Alic et al. 2012), while the equations of GRMHD are solved with a fourth-order high-resolution shock-capturing scheme (Del Zanna et al. 2007), together with a vector-potential-based constrained transport scheme inherited from the open-source code IllinoisGRMHD (Etienne et al. 2015). On the other hand, initial data is computed using the FUKA codes (Papenfort et al.

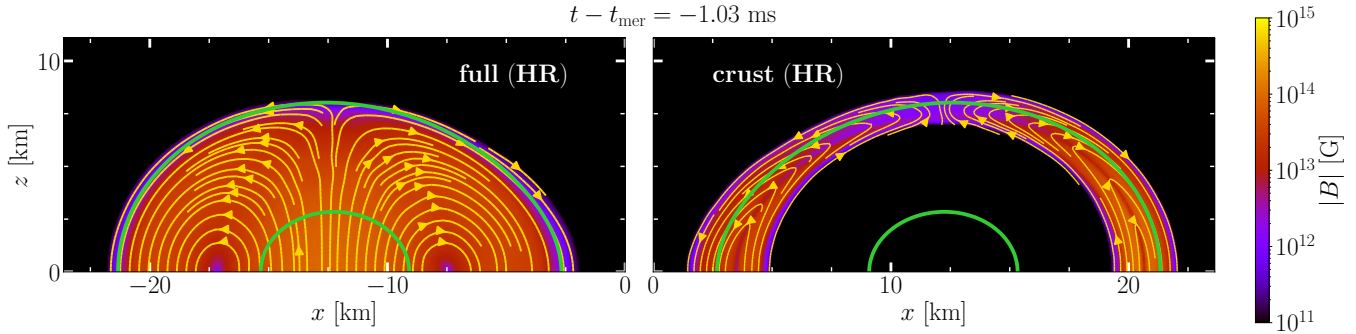


Figure 5. Distributions on the (x, z) plane of the magnetic-field strength $|B|$ from the HR simulations soon before merger. Magnetic-field lines are shown in yellow, while the left and right panels refer to the full- and crust-configuration, respectively.

Table 1. Characterising information on the different models explored in this work. We show the cell size on the highest refinement level, the seed magnetic-field parameters employed to initialize the magnetic field, the maximum magnetic-field strength after initialization, $|B|_{\max}^{\text{seed}}$, as well as the end time of the different stages discussed in the text, i.e. $t_{\text{end}}^{\text{KHI}}$, $t_{\text{end}}^{\text{D}}$ and $t_{\text{end}}^{\text{TA}}$, respectively.

Model	Δx [m]	R_{in} [M_{\odot}]	A_b	g_w [M_{\odot}^{-2}]	g_r [M_{\odot}]	p_{co} [M_{\odot}^{-2}]	n	$ B _{\max}^{\text{seed}}$ [G]	$t_{\text{end}}^{\text{KHI}} - t_{\text{mer}}$ [ms]	$t_{\text{end}}^{\text{D}} - t_{\text{mer}}$ [ms]	$t_{\text{end}}^{\text{TA}} - t_{\text{mer}}$ [ms]
full (HR)	70	0	0.028	0	0.0	1.0×10^{-8}	1.00	1.04×10^{14}	2.46	3.48	7.13
full (LR)	105	0	0.028	0	0.0	1.0×10^{-8}	1.00	1.04×10^{14}	1.77	5.15	10.1
crust (HR)	70	5	0.131	4	6.1	1.0×10^{-8}	0.85	2.36×10^{14}	0.90	3.59	5.09
crust (LR)	105	5	0.120	4	6.1	1.6×10^{-7}	0.85	2.26×10^{14}	1.82	3.54	11.5

2021) where the equal-mass binaries are chosen to be irrotational with a total ADM mass of $\sim 2.55 M_{\odot}$ initialized at a separation of $\sim 30 M_{\odot} \approx 44$ km. The computational grid has outer boundaries at $1000 M_{\odot} \approx 1476$ km in the three spatial directions and we employ a z -symmetry in the equatorial plane. We use seven refinement levels with factor of two refinement; the last level, which has a width of $32 M_{\odot}$, is added prior to merger, when the separation between the “barycenters” of the two stars is $\lesssim 9 M_{\odot}$.

Table 1 reports the smallest employed cell size Δx , the parameters of the initial magnetic field, the initial maximum magnetic-field strength $|B|_{\max}^{\text{seed}}$. Also reported are the times characterizing the different stages of our simulations, namely, the end of the KHI-driven stage $t_{\text{end}}^{\text{KHI}}$, the end of the decay stage $t_{\text{end}}^{\text{D}}$, and the end of the turbulent-amplification stage $t_{\text{end}}^{\text{TA}}$.

In analogy with, Fig. 2, we use Fig. 5 to offer a more intuitive view of the different topologies of the magnetic field also on the (x, z) plane. In particular, the figure reports the distributions of the magnetic-field strength $|B|$ from the HR simulations soon before merger. Magnetic-field lines are shown in yellow, while the left and right panels refer to the full- and crust-configuration, respectively; note that in both cases the magnetic field is purely poloidal.

Next, and in addition to what is already presented in Fig. 1, we discuss how the resolution impacts our results by contrasting the LR and HR version of the crust-configuration (we do not concentrate here on the full-configurations as these show very similar behaviour for both resolutions so that the discussion on full (HR) is applicable to full (LR), also these have been discussed in a number of papers, e.g., see Most et al. (2019) for a case with lower resolutions and higher magnetic-field strengths compared to the simulations in this work). Bearing in mind that the resolutions employed here do not allow for a rigorous convergence study, the overall evolution of the LR and HR-simulations provide evidence of being numerically consistent, i.e., that the errors should decrease with resolution. More specifically, Fig. 6 compares the HR (top row) at $t - t_{\text{mer}} = 0.52$ ms with the LR-simulations (bottom row) at $t - t_{\text{mer}} = 0.59$ ms, where the different times are due to the difference in phase evolution due to the different resolution. The first three columns from the left report the same quantities as shown in Fig. 3. The fourth column, on the other hand, reports the characteristic length-scale of the magnetic field, i.e., $|B|/|J|$, when expressed in units of resolution spacing Δx (see Eq. (15) of Obergaulinger et al. 2010). Here, $J := \sqrt{J^i J_i}$ and the spatial current is estimated as

$$J^i \simeq \frac{1}{4\pi\alpha} \epsilon^{ijk} D_j (\alpha B_k). \quad (1)$$

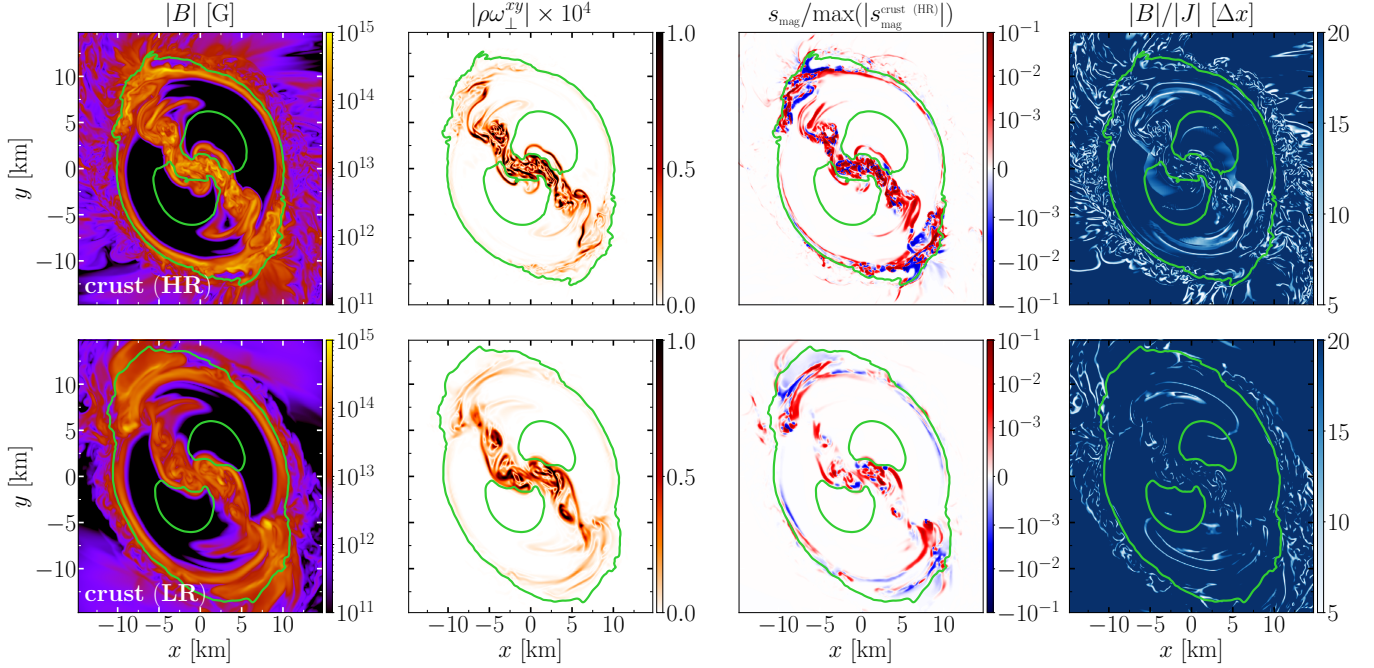


Figure 6. The first three columns from left as the same as in Fig. 3, while the fourth column reports the characteristic length-scale of the magnetic field, i.e., $|B|/|J|$, when expressed in units of resolution spacing Δx .

Expression (1) follows from the fact that in ideal-GRMHD the spatial components of the electric field can be expressed as $\alpha E_i = -\epsilon_{ijk} (v^j + \beta^j) B^k$, so that for nonrelativistic flows, $E_i \sim \mathcal{O}(v_i) \ll 1$ and the current reduces to Eq. (1).

Starting from the first column of Fig. 6 it is possible to realize that the HR simulation loses more magnetized material across the HMNS surface than the LR counterpart. This loss is most significant at both ends of the turbulent shear layer where also dynamical ejecta will originate from. The second column compares the densitized vorticity and shows that, as expected, more vorticity is present in the HR simulation and that the differences are more marked at both ends of the turbulent interface. The third column shows that stronger sinks (higher in magnitude but negative) are present at the ends of the turbulent interface in the HR simulation. Finally, the fourth column clearly shows that the HMNS in the HR simulation is surrounded by a “cloud” of low-density and magnetized material with a very small characteristic length-scale, which is not visible in the LR simulation. All in all, Fig. 6 illustrates how higher resolution for the crust-configuration can lead to enhanced shedding of highly magnetized material at the HMNS surface and hence that the magnetic-field amplification is bound to be smaller as opposed to the full-configuration.

REFERENCES

- Abbott, B. P., Abbott, R., Abbott, T. D., et al. 2017, *Phys. Rev. Lett.*, 119, 161101, doi: [10.1103/PhysRevLett.119.161101](https://doi.org/10.1103/PhysRevLett.119.161101)
- Aguilera-Miret, R., Viganò, D., Carrasco, F., Miñano, B., & Palenzuela, C. 2020, *Phys. Rev. D*, 102, 103006, doi: [10.1103/PhysRevD.102.103006](https://doi.org/10.1103/PhysRevD.102.103006)
- Aguilera-Miret, R., Viganò, D., & Palenzuela, C. 2022, *Astrophys. J. Lett.*, 926, L31, doi: [10.3847/2041-8213/ac50a7](https://doi.org/10.3847/2041-8213/ac50a7)
- Alic, D., Bona-Casas, C., Bona, C., Rezzolla, L., & Palenzuela, C. 2012, *Phys. Rev. D*, 85, 064040, doi: [10.1103/PhysRevD.85.064040](https://doi.org/10.1103/PhysRevD.85.064040)
- Anderson, M., Hirschmann, E. W., Lehner, L., et al. 2008, *Phys. Rev. Lett.*, 100, 191101, doi: [10.1103/PhysRevLett.100.191101](https://doi.org/10.1103/PhysRevLett.100.191101)
- Bernuzzi, S., & Hilditch, D. 2010, *Phys. Rev. D*, 81, 084003, doi: [10.1103/PhysRevD.81.084003](https://doi.org/10.1103/PhysRevD.81.084003)
- Chabanov, M., Rezzolla, L., & Rischke, D. H. 2021, *Mon. Not. R. Astron. Soc.*, 505, 5910, doi: [10.1093/mnras/stab1384](https://doi.org/10.1093/mnras/stab1384)
- Ciolfi, R. 2020a, *Mon. Not. R. Astron. Soc.*, 495, L66, doi: [10.1093/mnras/slaa062](https://doi.org/10.1093/mnras/slaa062)
- . 2020b, *General Relativity and Gravitation*, 52, 59, doi: [10.1007/s10714-020-02714-x](https://doi.org/10.1007/s10714-020-02714-x)
- Cowperthwaite, P. S., Berger, E., Villar, V. A., et al. 2017, *Astrophys. J. Lett.*, 848, L17, doi: [10.3847/2041-8213/aa8fc7](https://doi.org/10.3847/2041-8213/aa8fc7)
- Del Zanna, L., Zanotti, O., Bucciantini, N., & Londrillo, P. 2007, *Astron. Astrophys.*, 473, 11, doi: [10.1051/0004-6361:20077093](https://doi.org/10.1051/0004-6361:20077093)
- Drout, M. R., Piro, A. L., Shappee, B. J., et al. 2017, *Science*, 358, 1570, doi: [10.1126/science.aqa0049](https://doi.org/10.1126/science.aqa0049)

- Etienne, Z. B., Paschalidis, V., Haas, R., Mösta, P., & Shapiro, S. L. 2015, *Class. Quantum Grav.*, 32, 175009, doi: [10.1088/0264-9381/32/17/175009](https://doi.org/10.1088/0264-9381/32/17/175009)
- Fernández, R., Tchekhovskoy, A., Quataert, E., Foucart, F., & Kasen, D. 2019, *Mon. Not. R. Astron. Soc.*, 482, 3373, doi: [10.1093/mnras/sty2932](https://doi.org/10.1093/mnras/sty2932)
- Fujibayashi, S., Kiuchi, K., Wanajo, S., et al. 2023, *ApJ*, 942, 39, doi: [10.3847/1538-4357/ac9ce0](https://doi.org/10.3847/1538-4357/ac9ce0)
- Giacomazzo, B., Rezzolla, L., & Baiotti, L. 2009, *Mon. Not. R. Astron. Soc.*, 399, L164, doi: [10.1111/j.1745-3933.2009.00745.x](https://doi.org/10.1111/j.1745-3933.2009.00745.x)
- Giacomazzo, B., Rezzolla, L., & Baiotti, L. 2011, *Phys. Rev. D*, 83, 044014, doi: [10.1103/PhysRevD.83.044014](https://doi.org/10.1103/PhysRevD.83.044014)
- Giacomazzo, B., Zrake, J., Duffell, P. C., MacFadyen, A. I., & Perna, R. 2015, *Astrophys. J.*, 809, 39, doi: [10.1088/0004-637X/809/1/39](https://doi.org/10.1088/0004-637X/809/1/39)
- Gottlieb, O., Moseley, S., Ramirez-Aguilar, T., et al. 2022, *Astrophys. J. Lett.*, 933, L2, doi: [10.3847/2041-8213/ac7728](https://doi.org/10.3847/2041-8213/ac7728)
- Grandclément, P. 2010, *J. Comput. Phys.*, 229, 3334, doi: [10.1016/j.jcp.2010.01.005](https://doi.org/10.1016/j.jcp.2010.01.005)
- Kawamura, T., Giacomazzo, B., Kastaun, W., et al. 2016, *Phys. Rev. D*, 94, 064012, doi: [10.1103/PhysRevD.94.064012](https://doi.org/10.1103/PhysRevD.94.064012)
- Kiuchi, K., Cerdá-Durán, P., Kyutoku, K., Sekiguchi, Y., & Shibata, M. 2015a, *Phys. Rev. D*, 92, 124034, doi: [10.1103/PhysRevD.92.124034](https://doi.org/10.1103/PhysRevD.92.124034)
- Kiuchi, K., Kyutoku, K., Sekiguchi, Y., & Shibata, M. 2018, *Phys. Rev. D*, 97, 124039, doi: [10.1103/PhysRevD.97.124039](https://doi.org/10.1103/PhysRevD.97.124039)
- Kiuchi, K., Kyutoku, K., & Shibata, M. 2012, *Phys. Rev. D*, 86, 064008, doi: [10.1103/PhysRevD.86.064008](https://doi.org/10.1103/PhysRevD.86.064008)
- Kiuchi, K., Sekiguchi, Y., Kyutoku, K., et al. 2015b, *Phys. Rev. D*, 92, 064034, doi: [10.1103/PhysRevD.92.064034](https://doi.org/10.1103/PhysRevD.92.064034)
- Liu, Y. T., Shapiro, S. L., Etienne, Z. B., & Taniguchi, K. 2008, *Phys. Rev. D*, 78, 024012, doi: [10.1103/PhysRevD.78.024012](https://doi.org/10.1103/PhysRevD.78.024012)
- Löffler, F., Faber, J., Bentivegna, E., et al. 2012, *Class. Quantum Grav.*, 29, 115001, doi: [10.1088/0264-9381/29/11/115001](https://doi.org/10.1088/0264-9381/29/11/115001)
- Most, E. R., Jens Papenfort, L., Dexheimer, V., et al. 2020, *European Physical Journal A*, 56, 59, doi: [10.1140/epja/s10050-020-00073-4](https://doi.org/10.1140/epja/s10050-020-00073-4)
- Most, E. R., Papenfort, L. J., & Rezzolla, L. 2019, *Mon. Not. R. Astron. Soc.*, 490, 3588, doi: [10.1093/mnras/stz2809](https://doi.org/10.1093/mnras/stz2809)
- Murguía-Berthier, A., Ramirez-Ruiz, E., Montes, G., et al. 2016, *Astrophys. J. Lett.*, 835, L34, doi: [10.3847/2041-8213/aa5b9e](https://doi.org/10.3847/2041-8213/aa5b9e)
- Nathanail, A., Gill, R., Porth, O., Fromm, C. M., & Rezzolla, L. 2020, *Mon. Not. R. Astron. Soc.*, 495, 3780, doi: [10.1093/mnras/staa1454](https://doi.org/10.1093/mnras/staa1454)
- . 2021, *Mon. Not. R. Astron. Soc.*, 502, 1843, doi: [10.1093/mnras/stab115](https://doi.org/10.1093/mnras/stab115)
- Obergaulinger, M., Aloy, M. A., & Müller, E. 2010, *Astron. Astrophys.*, 515, A30, doi: [10.1051/0004-6361/200913386](https://doi.org/10.1051/0004-6361/200913386)
- Palenzuela, C., Aguilera-Miret, R., Carrasco, F., et al. 2022, *PhRvD*, 106, 023013, doi: [10.1103/PhysRevD.106.023013](https://doi.org/10.1103/PhysRevD.106.023013)
- Palenzuela, C., Lehner, L., Ponce, M., et al. 2013, *Phys. Rev. Lett.*, 111, 061105, doi: [10.1103/PhysRevLett.111.061105](https://doi.org/10.1103/PhysRevLett.111.061105)
- Palenzuela, C., Liebling, S. L., Neilsen, D., et al. 2015, *Phys. Rev. D*, 92, 044045, doi: [10.1103/PhysRevD.92.044045](https://doi.org/10.1103/PhysRevD.92.044045)
- Papenfort, L. J., Tootle, S. D., Grandclément, P., Most, E. R., & Rezzolla, L. 2021, *Phys. Rev. D*, 104, 024057, doi: [10.1103/PhysRevD.104.024057](https://doi.org/10.1103/PhysRevD.104.024057)
- Pons, J. A., & Geppert, U. 2007, *A&A*, 470, 303, doi: [10.1051/0004-6361:20077456](https://doi.org/10.1051/0004-6361:20077456)
- Pons, J. A., Miralles, J. A., & Geppert, U. 2009, *A&A*, 496, 207, doi: [10.1051/0004-6361:200811229](https://doi.org/10.1051/0004-6361:200811229)
- Price, D. J., & Rosswog, S. 2006, *Science*, 312, 719, doi: [10.1126/science.1125201](https://doi.org/10.1126/science.1125201)
- Radice, D. 2017, *Astrophys. J. Lett.*, 838, L2, doi: [10.3847/2041-8213/aa6483](https://doi.org/10.3847/2041-8213/aa6483)
- Rezzolla, L., Giacomazzo, B., Baiotti, L., et al. 2011, *Astrophys. J. Letters*, 732, L6, doi: [10.1088/2041-8205/732/1/L6](https://doi.org/10.1088/2041-8205/732/1/L6)
- Rezzolla, L., & Zanotti, O. 2013, *Relativistic Hydrodynamics* (Oxford, UK: Oxford University Press), doi: [10.1093/acprof:oso/9780198528906.001.0001](https://doi.org/10.1093/acprof:oso/9780198528906.001.0001)
- Ruiz, M., Tsokaros, A., & Shapiro, S. L. 2020, *PhRvD*, 101, 064042, doi: [10.1103/PhysRevD.101.064042](https://doi.org/10.1103/PhysRevD.101.064042)
- Schnetter, E., Hawley, S. H., & Hawke, I. 2004, *Classical and Quantum Gravity*, 21, 1465, doi: [10.1088/0264-9381/21/6/014](https://doi.org/10.1088/0264-9381/21/6/014)
- Siegel, D. M., Ciolfi, R., Harte, A. I., & Rezzolla, L. 2013, *Phys. Rev. D*, 87, 121302, doi: [10.1103/PhysRevD.87.121302](https://doi.org/10.1103/PhysRevD.87.121302)
- Takami, K., Rezzolla, L., & Baiotti, L. 2015, *Phys. Rev. D*, 91, 064001, doi: [10.1103/PhysRevD.91.064001](https://doi.org/10.1103/PhysRevD.91.064001)
- Togashi, H., Nakazato, K., Takehara, Y., et al. 2017, *Nucl. Phys.*, A961, 78, doi: [10.1016/j.nuclphysa.2017.02.010](https://doi.org/10.1016/j.nuclphysa.2017.02.010)
- Viganò, D., Garcia-Garcia, A., Pons, J. A., Dehman, C., & Graber, V. 2021, *Computer Physics Communications*, 265, 108001, doi: [10.1016/j.cpc.2021.108001](https://doi.org/10.1016/j.cpc.2021.108001)
- Zrake, J., & MacFadyen, A. I. 2013, *Astrophys. J.*, 769, L29, doi: [10.1088/2041-8205/769/2/L29](https://doi.org/10.1088/2041-8205/769/2/L29)